Article

n-Type PbSe Quantum Dots via Post-Synthetic Indium Doping

Haipeng Lu, Gerard M. Carroll, Xihan Chen, Dinesh K. Amarasinghe, Nathan R. Neale, Elisa M. Miller, Peter C. Sercel, Federico A. Rabuffetti, Alexander Efros, and Matthew C. Beard

J. Am. Chem. Soc., **Just Accepted Manuscript** • DOI: 10.1021/jacs.8b07910 • Publication Date (Web): 26 Sep 2018

n-Type PbSe Quantum Dots via Post-Synthetic Indium Doping

Haipeng Lu,[1] Gerard M. Carroll,[1] Xihan Chen,[1] Dinesh K. Amarasinghe,[2] Nathan R. Neale,[1] Elisa M. Miller,[1] Peter C. Sercel,[3] Federico A. Rabuffetti,[2] Alexander Efros,[4] and Matthew C. Beard[1*]

1. Chemistry & Nanoscience Center, National Renewable Energy Laboratory, Golden, Colorado 80401, USA
2. Department of Chemistry, Wayne State University, Detroit, Michigan 48202, USA
3. T. J. Watson Laboratory of Applied Physics, California Institute of Technology, Pasadena, California 91125, USA
4. Center for Computational Materials Science, Naval Research Laboratory, Washington DC 20375, USA

[*] Corresponding Author; email: matt.beard@nrel.gov

Abstract

We developed a post-synthetic treatment to produce impurity *n*-type doped PbSe QDs with In^{3+} as the substitutional dopant. Increasing the incorporated In content is accompanied by a gradual bleaching of the interband first-exciton transition and concurrently the appearance of a size-dependent, intraband absorption, suggesting the controlled introduction of delocalized electrons into the QD bandedge states under equilibrium conditions. We compare the optical properties of our In-doped PbSe QDs to cobaltocene treated QDs, where the *n*-type dopant arises from remote reduction of the PbSe QDs and observe similar behavior. Spectroelectrochemical measurements also demonstrate characteristic *n*-type signatures, including both an induced absorption within the electrochemical bandgap and a shift of the Fermi-level towards the conduction band. Finally, we demonstrate that the In^{3+} dopants can be reversibly removed from the PbSe QDs, whereupon the first exciton bleach is recovered. Our results demonstrate that PbSe QDs can be controllably *n*-type doped via impurity aliovalent substitutional doping.

TOC Graphics

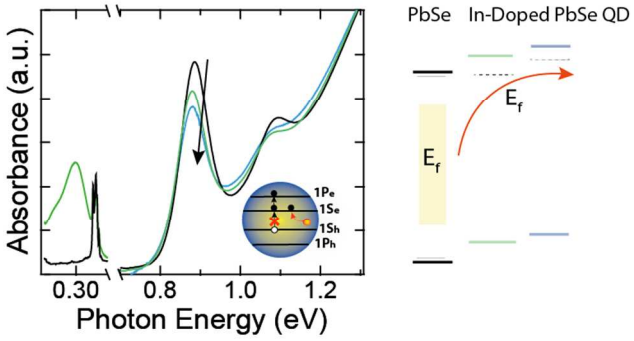

Introduction

Electronic impurity doping, which manipulates free-charge carriers in bulk semiconductors through the introduction of impurity atoms, has been one of the most important concepts for controlling the properties of semiconductors for a broad array of technologies.[1] Despite the maturity of electronic doping in bulk semiconductors, it remains a synthetic challenge to reliably incorporate and manipulate electronic impurity dopants into colloidal semiconductor nanocrystals, or quantum dots (QDs).[2] The injection of free-charge carriers into QDs has been previously demonstrated by remote chemical doping,[3-5] photochemical doping,[6-9] and electrochemical doping mechanisms,[10-12] all of which reveal characteristic spectroscopic signatures of electronically doped QDs. Although these electronic doping methods are fundamentally intriguing, practical implementation of QDs into optoelectronic devices, such as p−n junctions, diodes, transistors, solar cells, etc. would require a different approach that gives permanent, fixed electronic active QDs under equilibrium conditions.

Impurity doping of QDs via aliovalent cation substitution or interstitial incorporation has been demonstrated as a robust electronic doping method for QDs.[13-16] To date, electronic impurity doping can be achieved by single source precursors, nucleation doping, surface ligands, and partial cation exchange approaches.[17] However, it is often controversial whether the resulting colloidal QDs are electronically "doped" due to the so called "self-purification" mechanism that expels impurity atoms from the nanocrystal core to the nanocrystal surface giving electronic inactive impurity atoms.[18,19] This is evidenced by the lack of spectroscopic signatures of electronic impurity doping, that is i) a significant bleach of the first exciton transition due to band or state filling of $1S_e/1S_h$ state (via Pauli-blocking) and ii) the rise of an intense, size-dependent, low-energy intraband absorption stemming from the $1S_{h(e)}-1P_{h(e)}$ transition for *p*(*n*)-type doping.[2] While it is generally suggested that nucleation doping can lead to more uniform impurity doping in the ensemble of QDs,[17,20] post-synthetic cation exchange methods offers the ability to directly compare undoped and subsequently doped QDs. Recently, we developed a facile post-synthetic partial cation exchange process that allows controllable Ag^+ doped PbSe QDs (Ag:PbSe).[16] As we reported in our earlier work,[16] we found that the incorporation of Ag^+ into PbSe QDs proceeds *via* a substitutional doping mechanism, where Ag^+ cations replace Pb^{2+} cations within the PbSe lattice. The Ag^+ dopants inject excess free-holes into the $1S_h$ bandedge states, as confirmed by a gradual bleach of the first-exciton interband transition strength and the concurrence of a size-dependent intraband absorption. We found that an average of 1-hole per QD requires ~10% Ag^+ incorporation. However, the majority of the incorporated Ag^+ remains at the QD surface in electronically inactive sites. A dynamic equilibrium between surface and core Ag^+ achieve stable *p*-type doping behavior, where the active Ag^+ dopant concentration is less than 1%. Given that the as-synthesized PbSe QDs are typically *p*-type because of partial surface oxidation, it seems compelling to prepare *n*-type QDs using aliovalent impurity doping.

Herein, we develop electronic impurity *n*-type doping of PbSe QDs using a post-synthetic In^{3+} partial cation exchange (In:PbSe QDs) under ambient conditions. Subsequent structural, optical and electronic properties of the In-incorporated PbSe QDs are studied. Optical absorbance measurements show a gradual bleach of the first-exciton interband transition strength, which correlates linearly with the incorporated In-content. Concurrently, we observe the appearance of quantum-confined, NIR intraband absorbance, whose transition energies match those found using remotely doped (cobaltocene) QDs, further confirming the free-carrier populated quantized states ($1S_e$) in the doped samples. Quantitative powder X-ray diffraction (XRD) analysis displays a linear correlation between lattice parameters and dopant concentration (Vegard's law), suggesting substitutional doping. Spectroelectrochemical measurements demonstrates that the substitutional In^{3+} atoms act as *n*-type dopants in PbSe QDs.

Results

A. Doping Efficiency and Mechanism

PbSe QDs were doped post-synthetically with In^{3+} via an adapted procedure from Ag:PbSe QDs.[16] This is achieved by the addition of a small amount of a concentrated $In(NO_3)_3$ or $InCl_3$/methanol solution into stirred solutions (in hexanes) of PbSe QDs at room temperature. The incorporation of In is quantitatively determined by inductively coupled plasma optical emission spectroscopy (ICP-OES). We find that approximately 50% of the added In is incorporated into the purified PbSe QDs, which is close to that found for our Ag-doping procedure. The In-incorporation efficiency does not depend strongly on the QD size (**Fig. 1a**), which differs from that found for the Ag case, where Ag incorporates more easily into larger particles. The highest In-incorporation is around 4% relative to Pb after which the In-doped PbSe QDs become colloidally unstable. TEM images display an increased particle aggregation with higher In contents, indicating a removal of surface ligands due to the $In(NO_3)_3$/methanol addition. We carefully conducted quantitative ^1H NMR experiments to elucidate the In-doping mechanism. Neat methanol can strip off surface oleate ligands because of its acidity,[21] and we find that by itself leads to a ~30–40% loss of surface oleate ligands (**Fig. 1b**). Since the surface coverage of organic ligands plays an essential role in both the QD optical and electronic properties, we always use neat methanol as a control experiment for the characterizations presented herein. The addition of $In(NO_3)_3$/methanol further promotes the loss of oleate ligands, and we find that with every incorporated In^{3+} cation there is a displacement of around 2 oleate ligands (**Fig. 1b**). Therefore, we hypothesize that the In-doping mechanism proceeds through a Z-type neutral-acceptor surface-ligand exchange[22] with the loss of $Pb(oleate)_2$ (**Scheme 1**) and the incorporation of $In(NO_3)_3$ or $InCl_3$. Consistent with our proposed

mechanism, we find, in the ICP-OES data (Supporting Information), a decrease in the atomic ratio of Pb-to-Se as the In-content increases.

Scheme 1

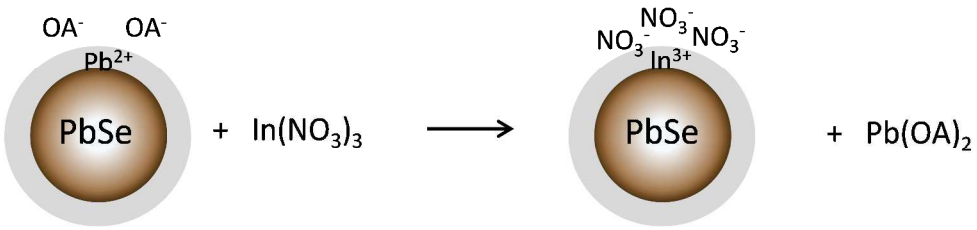

$[Pb(OA)_2]_x(PbSe)_n[Pb(OA)_2] + In(NO_3)_3 \rightarrow [Pb(OA)_2]_x(PbSe)_n[In(NO_3)_3] + Pb(OA)_2$

The similar In^{3+} incorporation efficiency to that found for Ag^{+}, in our prior work, suggests an analogous doping mechanism, that is, substitutional doping *via* intraparticle cation-exchange between surface-bound In^{3+} and Pb^{2+}-core cations. However, the significant difference of ionic radius between Pb^{2+} (133 pm) and In^{3+} (94 pm) might promote interstitial doping, producing *p*-type PbSe QDs, rather than the desired *n*-type. To verify substitutional doping, we performed quantitative powder XRD analysis using the General Structure Analysis System software (GSAS) with the graphical user interphase EXPGUI.[23,24] The quality of the refined structure model was assessed by R_{wp} residuals and difference curves. As the R_{wp} residuals of all refinements are <3% (**Fig. S2**), the lattice constant can be extracted from the structure model with extraordinary fidelity. As expected for substitutional doping, we find that the incorporation of In^{3+} does not significantly alter the crystal structure of cubic PbSe (**Fig. 2a**). In addition, the calculated lattice constant monotonically decreases with increasing In concentration, in close agreement with Vegard's law (**Fig. 2b**). As the ionic radius of In^{3+} is smaller than Pb^{2+}, the reduced lattice constant suggests In^{3+} cations replace Pb^{2+} cations. If In-atoms resided in interstitial sites, we would observe a lattice expansion with increasing In-content.

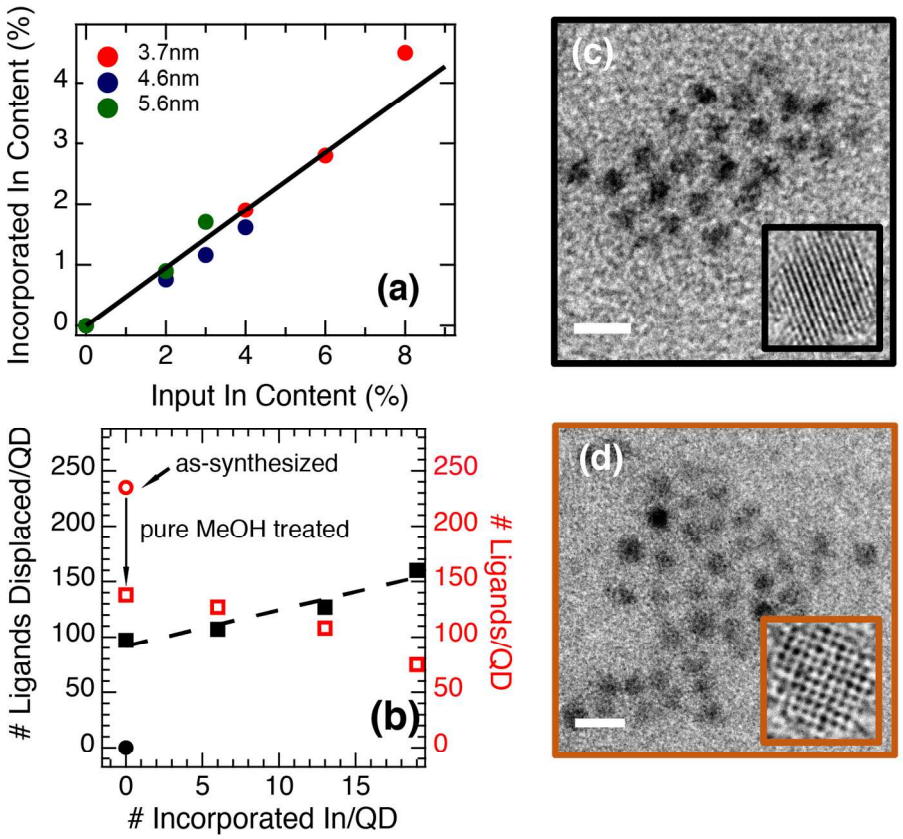

Figure 1. (a) Summary of ICP-OES data showing the ratio of incorporated In to input In is approximately 50% (black-trace), and no strong dependence on QD size. (b) Quantitative ^{1}H NMR measurements indicate the loss of surface oleate ligands with increasing of In incorporation (d = 4.2 nm). (c-d) TEM images of as-synthesized and In-doped PbSe QDs, respectively. Scale bars are 10 nm.

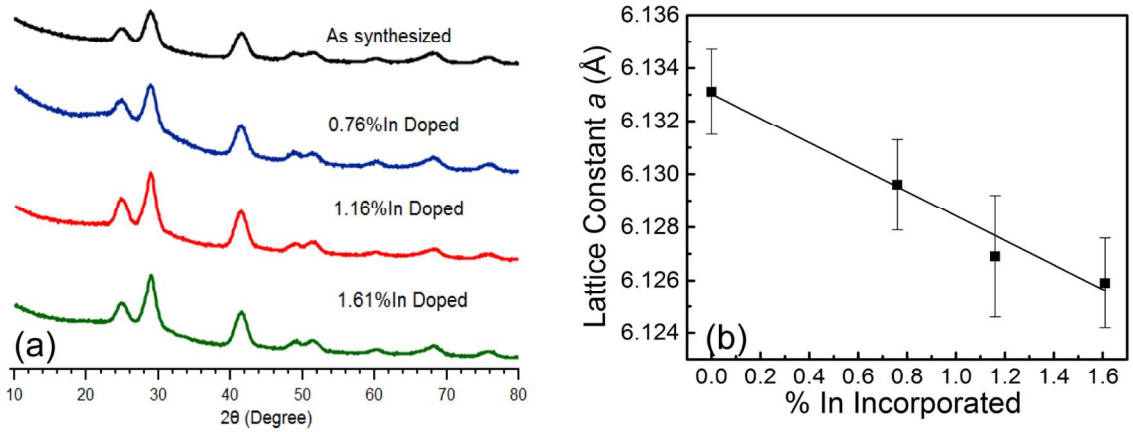

Figure 2. (a) XRD patterns of 4.6 nm In:PbSe QD samples. (b) Calculated lattice constant vs incorporated In content (data points; 0–1.6%).

B. Bleaching of Exciton Transitions

The successful introduction of substitutional In^{3+} in the PbSe nanocrystal lattice should result in excess delocalized electrons.[2] We can readily assess the substitutional doping efficiency by monitoring the change in optical absorbance of the first exciton transition ($1S_h$–$1S_e$). We find that the first exciton interband transition strength is gradually quenched as the In content increases with a small red-shift for the highest In incorporation (**Fig. 3a**). All spectra are normalized in the spectral range of ~1.8 eV to ~2.2 eV where the oscillator strength only relies on the concentration of intrinsic (core) PbSe QDs. The bleach of the absorbance spectra is not due to the addition of neat methanol or NO_3^- ions (**Fig. S3**). The delocalized electron concentration can be quantified based on the bleach of $1S_h$–$1S_e$ interband transition, $\Delta\alpha/\alpha$, assuming a Poisson distribution and a degeneracy of 8. The normalized bleach is calculated as $\Delta\alpha/\alpha = \sum_{m=1}^{8} m \cdot P_m/8 + \sum_{m=9}^{\infty} P_m$, where $P_m = \langle N_e \rangle^m \; exp(-\langle N_e \rangle)/m!$ and $\langle N_e \rangle$ is the average number of delocalized electrons induced by the In^{3+} dopants per QD. The calculated $\langle N_e \rangle$ for various sizes of doped PbSe QDs (**Fig. 3b)** serve as an estimation for the electronic impurity doping efficiency. Interestingly, we find that it is more efficient to introduce delocalized carriers in larger QDs with the same amount of In incorporation. For instance, with the same In-incorporated of ~0.9%, doped PbSe QDs gives on average 1.2, 1.0, and 0.43 delocalized electrons in 5.6 nm, 4.6 nm, and 3.7 nm QDs, respectively. The reduced efficiency can be attributed to a larger surface/volume ratio in the smaller QDs, where it is more thermodynamically favorable to expel impurity atoms to the QD-surface, thus needing more In^{3+} to induce a stable core-In^{3+} population.[16] It can also be related to lower Pb:Se ratios (**Table S1**), thus higher Pb^{2+} vacancies in larger QDs, since dopants can diffuse more rapidly through existing cation vacancies. Furthermore, the apparent doping efficiency of In^{3+} is much higher than that found for Ag^+. For Ag, ~ 10% of the Pb is replaced by Ag in order to achieve 1 hole/QD; here, only 1–2% of In substitution is required to produce 1 electron/QD. The difference in substitutional doping may be related to the surface-for-core cation exchange mechanism, with the smaller In^{3+} (94 pm) versus Ag^+ (115 pm) likely resulting in a lower energy pathway through the PbSe lattice.

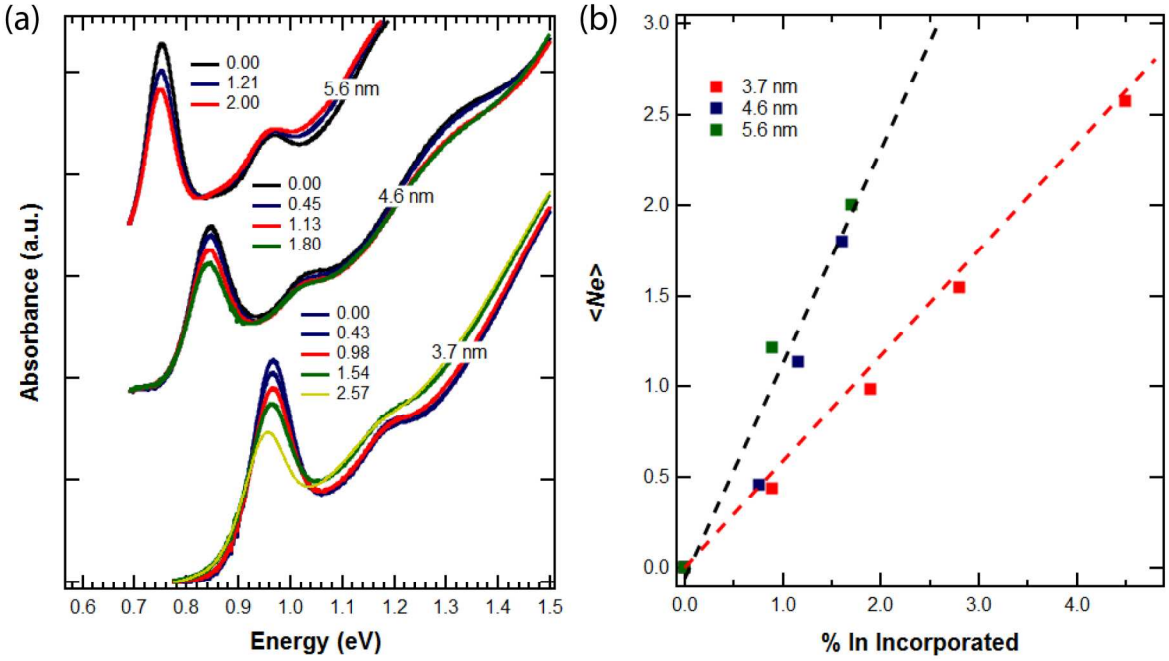

Figure 3. (a) Absorbance spectra of PbSe QDs solutions for QDs of diameters of 3.7 nm, 4.6 nm, and 5.6 nm with increasing In content. The average number of free electrons, $<N_e>$, determined from the bleach magnitude is denoted. (b) Plot of $<N_e>$ vs the incorporated In-content.

C. Size-Dependent Intraband Absorption

As reported previously by electrochemical[11], photochemical[7,25], and remote-doping approaches[4], delocalized carriers in QDs exhibit both an interband bleach and a quantum-confined, low-energy intraband absorption arising from the $1S_{h(e)}$–$1P_{h(e)}$ transition for *p*(*n*)-type doping. Here, we also observe a broad IR absorption band in In:PbSe QDs (**Fig. 4a**, top, black-trace is the as-prepared QDs and red-trace is the In:PbSe doped QDs). The IR absorption is measured by Diffuse Reflectance Infrared Fourier Transform Spectroscopy (DRIFTS). The identity of the observed IR band can be assigned by comparing with cobaltocene-treated PbSe QDs. Cobaltocene has been reported to transfer electrons (remotely) to the $1S_e$ state of PbS(e) QDs, giving a characteristic NIR absorption band from the resulting *n*-type QDs.[4] Accordingly, the NIR absorption band in cobaltocene-treated PbSe QDs is assigned to the $1S_e$–$1P_e$ transition, and is utilized here as an established control (**Fig. 4a**, bottom, black-trace is the as-prepared QDs and blue-trace is after the cobaltocene treatment). We find that the NIR absorption band in the $InCl_3$-treated PbSe QDs possesses approximately the same energy as that of cobaltocene-treated PbSe QDs, and it is consistent for different sizes of PbSe QDs (**Fig. 4b,** blue and green squares). Therefore, we assign the NIR absorption band of the In:PbSe QDs to the $1S_e$–$1P_e$ transition due to increased carrier population in the $1S_e$ state upon In^{3+} incorporation. We note that all DRIFTS measurements are conducted under strict air-free conditions using oxygen- and water-free solvents; as the intraband absorption rapidly disappears upon air exposure. We also find good agreement with the work of Guyot-Sionnest and co-workers who studied

electronically doped PbSe QD films using electrochemical doping (**Fig. 4b**, open-purple square[11]). The results from Klimov and co-workers who studied remote doping using the same cobaltocene treatment as used here (**Fig. 4b**, open green square)[4] also agrees with our results. We calculated the $1S_e$–$1P_e$ transition energy using the standard $k \cdot p$ calculation based on the Kang and Wise[26] method and find good agreement (black dashed-trace **Fig. 4b**). Here we applied a constant correction factor to the QD diameter to ensure that the calculated interband transition energies match our sizing curve.[27]

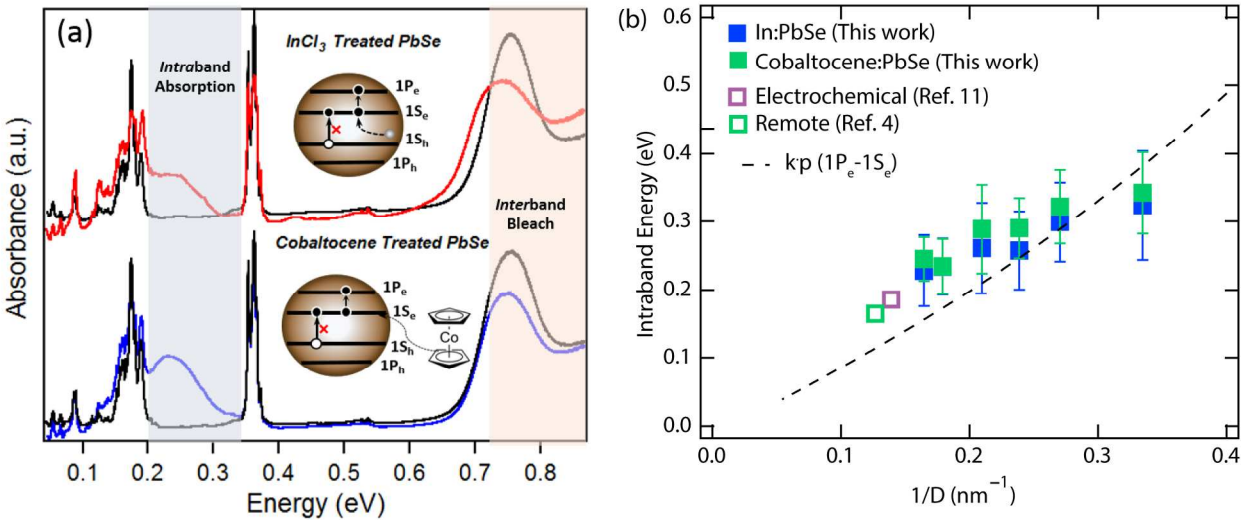

Figure 4. (a) DRIFTS absorbance spectra of 5.6 nm PbSe QD films. The QD cartoon schematic represents the optical transitions expected for In:PbSe QDs. The optical signatures, which are the bleach of the interband and the appearance of intraband absorption, are observed in both $InCl_3$-treated and cobaltocene-treated PbSe QDs. The intraband energies of these two different treatments appear to be the same. (b) Observed size-dependent intraband energy $1S_e$–$1P_e$: In-doped (filled blue squares); cobaltocene-treated (filled green squares); remote-doped from literature (open green square)[4]; electrochemical doped from literature (open purple square).[11] Compared to calculated intraband energies: dashed-black trace is the $1S_e$-$1P_e$ transition energy calculated from the standard $k \cdot p$ theory of Kang and Wise.

D. Spectroelectrochemical Measurements

To gain insight into the electronic behavior of In:PbSe QDs, spectroelectrochemical measurements were conducted on as-cast QDs films without any additional ligand exchange (usually employed to make conductive QD-arrays, but can also impact the doping). In a spectroelectrochemical measurement the differential absorbance ($\Delta A/A_0$) of the QD film deposited onto an FTO electrode is measured as a function of an applied potential, V_{app}, between the working FTO electrode and Ag reference electrode. Here, $\Delta A = A_{V_{app}} - A_0$, and $A_{V_{app}}$ is the absorption at V_{app}, and A_0 is the absorption under open circuit conditions (no current flow), or V_{oc}. The peak of the wavelength dependent $\Delta A/A_0$ is plotted as a function of V_{app} (**Fig. 5b** and **5c**) giving a spectroelectrochemical characteristic response. In **Fig. 5a** we show

three typical differential absorption spectra of 4% In:PbSe QDs at V_{app} of −0.95 V, −0.70 V, and −0.15 V vs. Ferrocenium/Ferrocene (Fc^+/Fc) and the differential absorption at 1450 nm (peak of the bleach feature) for each V_{app} is plotted (**Fig. 5b**). At the most negative potential, −0.95 V vs Fc^+/Fc, the excitonic absorption at λ = 1450 nm is nearly bleached, giving a $-\Delta A/A_0$ close to 1 (**Fig. 5a**, spectra X); this results from an increase in the population of delocalized conduction band electrons injected from the electrode. As the applied potential is swept positive, the absorption recovers, and the differential absorbance decreases, until $\Delta A/A_0 = 0$ at $V_{App} \approx -0.7$ V vs Fc^+/Fc (**Fig. 5a**, spectra Y). This corresponds to the intrinsic Fermi-level, E_f, of the QD thin film under open circuit conditions. Upon further oxidative bias, an induced absorption of $\Delta A/A_0$ = 0.2 is observed (**Fig. 5a**, spectra Z). The induced absorption arises as a result of removing conduction band electrons initially present due to In-substitutional doping. With additional positive electrode potential, $-\Delta A/A_0$ increases again resulting from hole-injection into the valence band.

We next compare the spectroelectrochemical response of the 4% In:PbSe QDs to intrinsic PbSe, and PbSe with higher indium content (6%) (**Fig. 5c**). The differential excitonic absorption of intrinsic PbSe QDs (**Fig. 5c**, red-circles) displays both *p*- and *n*-type character.[11,33,34] Between −0.55 V and −0.85 V, $-\Delta A/A_0$ increases with increasingly negative potential as electrons are injected into the conduction band. For potentials more negative than −0.85 V, the $-\Delta A/A_0$ plateaus, where the $1S_e$ level of the conduction band is filled by electrons. Increasingly positive potentials (greater than −0.05 V) also results in an increase in $-\Delta A/A_0$, and is assigned to hole-injection into the valence band. Between 0.0 V and −0.55 V, $-\Delta A/A_0 \approx 0$, where the absence of an induced absorption indicates no appreciable charge injection/extraction. The number of electrons injected into the conduction band are dictated by the applied voltage:

$$n_e = \int_0^\infty \rho_c(E)\left(1 - f\left(E; V_{app}\right)\right) dE, \quad (1)$$

where ρ_c is the density of conduction band states and is taken as, $8 \cdot G(E; E_c)/V_{NC}$, where $G(E; E_c)$ is a normalized Gaussian function centered at the conduction band edge, E_c.

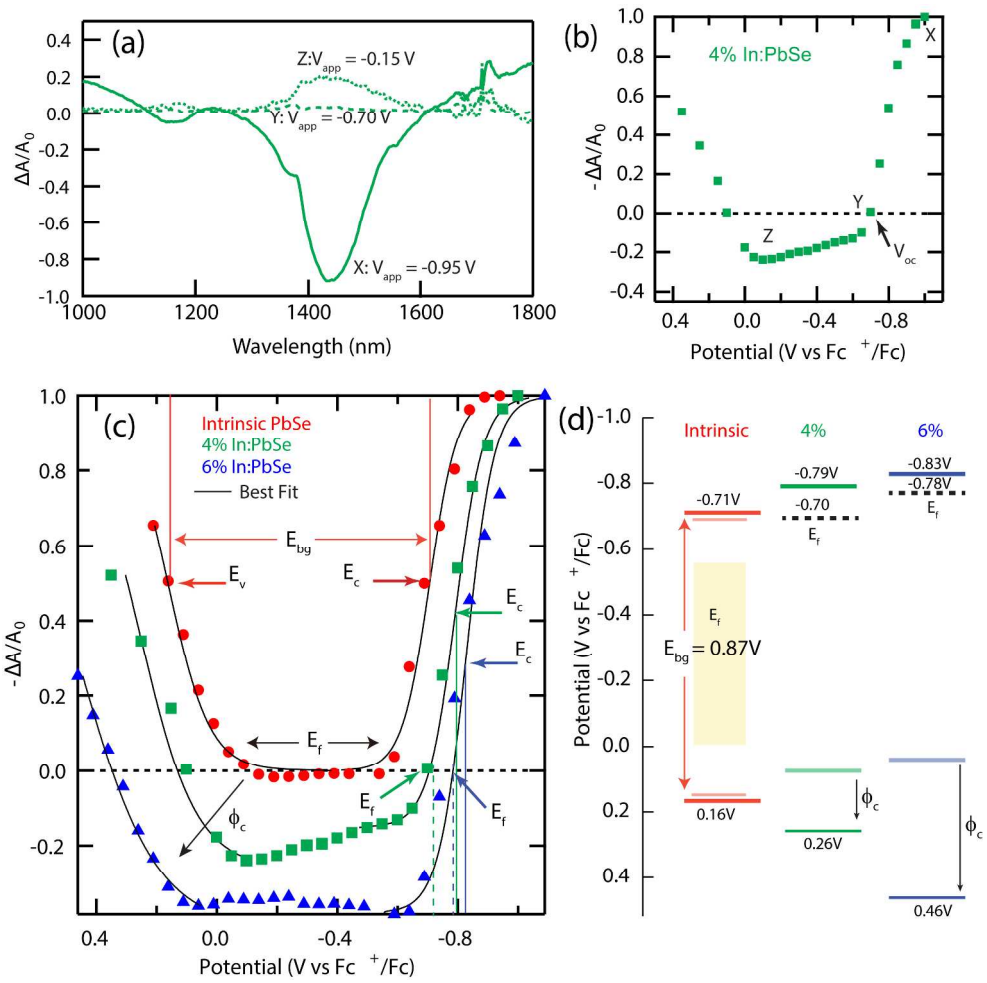

Figure 5. (a) Normalized differential absorption spectra of *d* = 4.3 nm 4% In:PbSe QDs deposited as a thin film on FTO in 0.1 M $LiClO_4$ in acetonitrile. The spectra were collected under electrochemical bias at V_{App} = −0.95 V (solid), −0.70 V (dashed), and −0.15 V (dotted) in a three-electrode configuration. (b) Differential excitonic absorption at 1450 nm of 4% In:PbSe QD thin films in 0.1 M $LiClO_4$ in acetonitrile as a function of the electrochemical bias. X, Y, Z points correspond to V_{App} = −0.95 V, −0.70 V, and −0.15 V respectively. (c) Normalized differential excitonic absorption of intrinsic PbSe (red-circles), 4% In:PbSe (green-squares), and 6% In:PbSe (blue-triangles) QD thin films as a function of the electrochemical bias. All potentials are referenced against the experimentally determined Ferrocenium/Ferrocene (Fc^+/Fc) redox couple. (d) Energy diagram of PbSe QDs with respect to Fc^+/Fc redox couple. The Fermi-level shifts to more negative values (−0.7 and −0.78 V) for the 4 and 6% samples. The difference between E_f and the conduction band is smaller for the 6% sample; ($\Delta E_f = E_c - E_f$), and ΔE_f is 0.09 V for the 4% sample, and 0.05 V for the 6% sample. The E_f of intrinsic PbSe QDs can only be specified in our experiment with an upper limit of ~−0.55 V and lower limit of ~ 0.0V (shaded area for intrinsic PbSe QDs). The onset for hole-injection into the valence band, increases by ~ 200 mV from intrinsic PbSe to 6%In:PbSe (denoted as ϕ_c). Overall, increasing In content in PbSe QDs leads to more *n*-type character (smaller ΔE_f).

The Fermi-function, $f(E; V_{app})$ is defined as usual (see Supporting Information). The NC volume, V_{NC}, drops out of Eq. 1 because $n_e = N_e/V_{NC}$ where N_e is the number of electrons per QD. The number of injected holes as a function of applied voltage can be similarly defined to

determine the valence band edges. Note when $V_{app} = E_c$, $N_e = 4$, and the conduction band level is half full (points marked on **Fig. 5c**). From a best-fit of Eq. 1 to the data (**Fig. 5c**, black-traces) we extract the conduction and valence band edges for each of the samples (data summarized in **Fig. 5d**). For the undoped sample, E_c = −0.71 V and E_v = 0.16 V, giving an electrochemical bandgap of E_{BG} = 0.87 V, which is slightly higher than the 0.86 eV optical bandgap.

The spectroelectrochemical response of the doped samples display the same general shape as the intrinsic sample, but with three important differences expected for defect-related *n*-type doping. First, as discussed above, $\Delta A/A_0$ becomes positive within the voltammetric window, and the induced absorption increases with increasing In^{3+} content, $\Delta A/A_0$ = 0.14 and 0.35 for the 4% and 6% In:PbSe QDs, respectively. The positive $\Delta A/A_0$ arises from 'de-doping' the QDs and thereby restoring the bleached absorption. Thus, the value of $-\Delta A/A_0$ in the plateau region is proportional to the average number of conduction band electrons, $\langle N_e \rangle$, introduced from In^{3+} doping. We estimate, $\langle N_e \rangle$ = 1.1 for the 4% and 2.8 for 6% sample; close to that estimated from the bleach of the linear absorption spectrum, (**Fig. S4**). The second characteristic is the increasingly negative position of E_f with respect to E_c with higher In content. The difference between E_f and E_c (ΔE_f) of the 4% and 6% In:PbSe are −0.09 and −0.05 V, respectively. The diminishing ΔE_f indicates an increasing conduction band electron concentration which pushes E_f closer to E_c. From ΔE_f, we calculate the doping density per QD, to be 1.1 and 2.3, consistent with the other estimates of the doping density described above. The final spectroelectrochemical characteristic is that the onset for hole-injection into the valence band, increases by ~ 200 mV from intrinsic PbSe to 6% In:PbSe (denoted as ϕ_c). The additional potential for hole injection results from an increased coulombic repulsion between the non-charge compensated In^{3+} defects and electrochemically injected delocalized holes.

While the electron injection potential at the conduction band edge is expected to shift positive due to enhanced coulombic stabilization from internal In^{3+},[36] our data shows the opposite; the conduction band shifts to slightly more negative potentials with increasing doping (−0.71 for the undoped, and −0.79 and −0.83 V for the 4% and 6% samples). The origin of this negative shift may be from an altered QD ligand shell,[35] residual NO_3^- ions at the QD surface which dictate the "Charged Sphere" potentials,[36] or decreased Pb/Se surface stoichiometries.[37,38] In all cases, the surface of the QDs likely dictates the absolute bandedge potential, and in our experiments, the chemical environment at the QD surface of the doped samples are different than those of the undoped. Thus it is not surprising to observe negatively shifted conduction band edge potentials.

E. Photoluminescence and Time-resolved Absorption Spectroscopy

We find that the photoluminescence quantum yield (PLQY) significantly drops as the In concentration increases (**Fig. 6**, blue-squares), indicating additional non-radiative decay paths.

Since the addition of neat methanol also results in loss of surface oleate ligands (**Fig. 1b**) which could introduce excess surface traps, the absolute PLQY was reduced from 16% (as-synthesized PbSe) to 13% (methanol-treated PbSe QDs). Therefore, to better compare the PLQY of doped and undoped QDs, we again use neat methanol-treated PbSe QDs (**Fig. 6**, red-square) as an initial reference for undoped QD, which accounts for the induced surface traps. The loss of PLQY of In-doped QDs can then be attributed to the In incorporation in QDs. Assuming that the QDs that are doped, within the Poison distribution of $\langle N_e \rangle = 0.43$, do not emit, we expect about 35% decrease of the absolute PLQY. We observe a reduction of ~30% in reasonable agreement to our prediction.

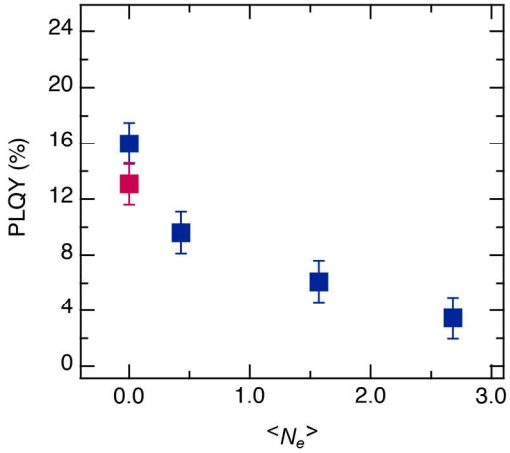

Figure 6. PLQY as a function of the number of delocalized electron in PbSe QDs. The red square dot represents the PLQY of neat methanol treated PbSe QDs.

Transient absorption (TA) spectroscopy[16,39] was applied to probe the exciton decay kinetics of 3.7 nm as synthesized and In-doped PbSe QD solution samples in tetrachloroethylene (TCE). Normalized TA kinetics for the various In:PbSe QD samples under identical laser excitation fluence (**Fig. 7)**. The pump wavelength was set to 700 nm, well below the threshold of multiple exciton generation (MEG) for these QD samples, and the pump fluence was adjusted to generate ~0.016 absorbed photons per pulse per QD, so no biexcitons are photoexcited during the experiment (i.e., the observed decay originates from single excitons only). As the In-dopant content increases, we observe a faster decay of the exciton population, suggesting a new, nonradiative relaxation pathways with increased doping concentration.

To rationalize the data, we assigned the decreased exciton lifetime to the presence of In dopants.[16] When the QDs are not doped, no electronic dopants are present, the kinetics of exciton decay can be fitted with a single exponential function with 1.22 μs. When QDs are doped with In, an additional exponential component with the time constant of 76.2 ns is needed to best fit the kinetics. All of the transients for the differently doped samples can now be modeled simultaneously using the following function:

$$\frac{\Delta\alpha}{\alpha} = A_0 e^{\frac{-(t-to)}{\tau_0}} + A_1 e^{\frac{-(t-to)}{\tau_1}} \qquad (2)$$

Where τ_0 represents the intrinsic lifetime of 1.22 μs of undoped QD and τ_1 represent exciton lifetime of 76.2 ns in the presence of the dopants. We observe a rise of the amplitude of τ_1 as the doping concentration increases.

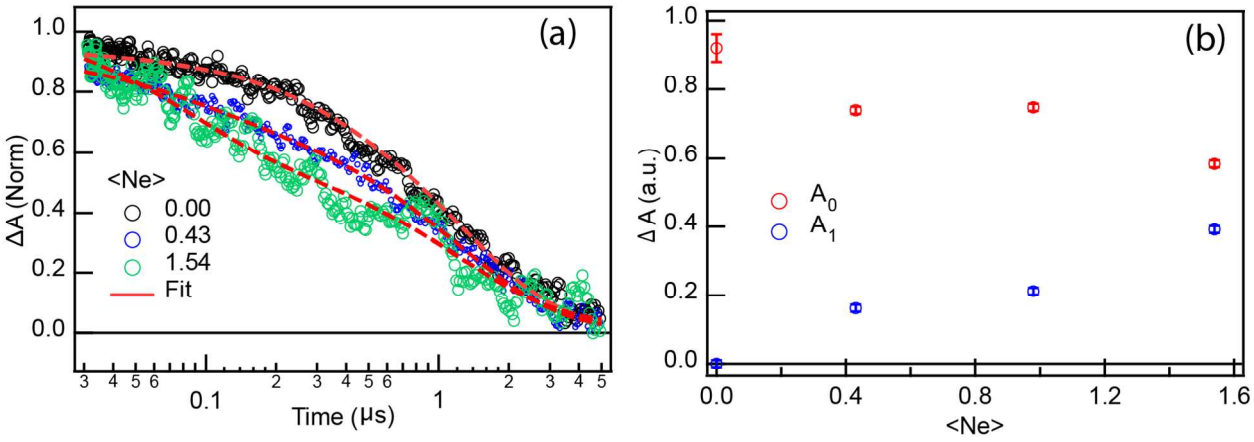

Figure 7. (a) Normalized decay dynamics of as synthesized and In:PbSe 3.7 nm QDs. The undoped QDs have a single exponential lifetime of 1.22 μs and the doped QDs have an additional exponential lifetime of 76.2 ns. The dashed red traces are the results of the fit discussed in the text. (b) The amplitude of exponential decay component. A_0 is the amplitude associated with the undoped component and A_1 is the amplitude associated with electronic doped component. As the electronic doping increases, the amplitude associated with electronic doping also increased.

Discussion

Our data clearly indicates that *n*-type PbSe QDs are achieved through post-synthetic $In(NO_3)_3$ (or $InCl_3$) treatment via a substitutional mechanism, where In^{3+} acts an interior electron donor. The impurity doping process is initiated at the QD surface through a Z-type ligand exchange reaction, followed by diffusion of In^{3+} cations and core-lattice Pb^{2+} substitution,[40] as proposed in our Ag^+ *p*-type PbSe QD doping report.[16] These two elementary steps give 'surface-doped' and 'interior doped' QDs, respectively, and can be well tailored by reaction conditions (*e.g.,* temperature, surface ligands) via controlling ion diffusion rates. The partial removal of surface Pb-oleate ligands by methanol can enhance the surface exposure to In^{3+}, assisting the subsequent second step of indium incorporation. The high diffusivity nature of In^{3+} enables facile incorporation into PbSe QDs at room temperature. While the rapid diffusion allows a convenient doping mechanism, it also promotes a reverse out-diffusion process. That is, the doping mechanism is thermodynamically reversible. For instance, when $Pb(oleate)_2$ is added to the In:PbSe QDs, the excitonic bleach observed for the In:PbSe recovers almost entirely back to the pristine PbSe QDs (**Fig. 8**), indicating a In^{3+} de-doping process. A ligand-assisted dopant out-diffusion has been previously observed in Cu^+-doped CdSe QDs.[41,42] Therefore, the surface chemistry of doped QDs plays a critical role in stabilizing electron impurity dopants, and extra

caution must be taken when characterizing the *n*-type nature of In:PbSe films. In fact, when ultraviolet photoelectron spectroscopy (UPS) and X-ray photoelectron spectroscopy (XPS) were performed on both PbSe and In:PbSe QDs to probe the shift of the QD Fermi-level, we were not able to gain any insightful results on the valence band maximum due to the high sensitivity of surface treatments on doped QDs (**Fig. S5**). For this reason, all of our spectroscopic characterization were conducted with native-ligand-capped PbSe and In:PbSe QDs.

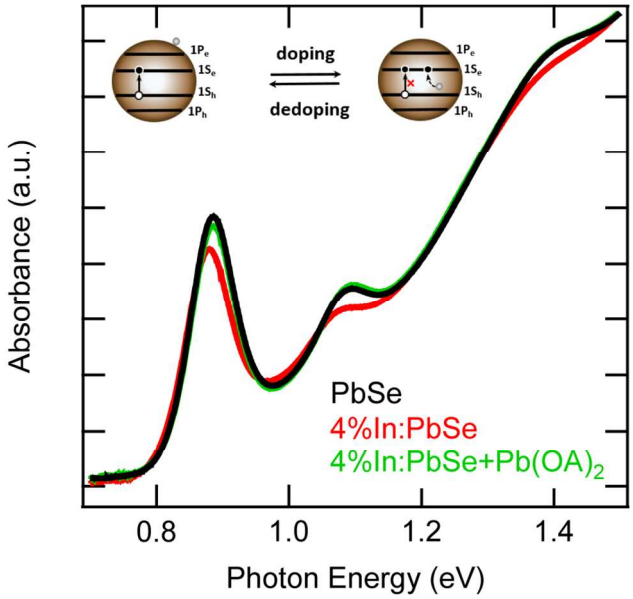

Figure 8. (a) Normalized absorbance spectra of pristine, 4% In doped, and de-doped PbSe QDs solutions, respectively. De-doped PbSe QDs was achieved by adding excess Pb(oleate)$_2$ ligands to In:PbSe QDs.

Although the intraband energy of *n*-doped, electronic-active PbSe QDs has been previously reported, we measured the *size-dependent* intraband ($1S_e$–$1P_e$) energies of PbSe QDs (**Fig. 4b**). Such size-dependent intraband analysis can be quite useful to the understanding of the electronic structure of QDs, such as, the assignment of the 2nd exciton peak, which has been the subject of much discussion. The good agreement between k.p calculations, measured intraband transition energies, and the difference in the 1st and 2nd exciton energies has been used to conclude that the 2nd exciton peak in the linear absorption spectrum arises from a dipole forbidden $1S_h$–$1P_e$/$1P_h$–$1S_e$ transition.[44-46] However, this conclusion contradicts other experimental observations[47,48] which assign the second exciton peak to a dipole allowed $1P_h$–$1P_e$ transition energy. Most notably, recent work from Gamelin and co-workers who studied photodoped PbSe QDs and concluded that the second exciton must arise from the $1P_h$–$1P_e$ transition, under heavy doping conditions they observe a new peak between the 1st and 2nd excitons and assign that peak to the $1S_h$-$1P_e$/$1P_h$-$1S_e$.[25] To illustrate, we plot estimates of the intraband transition energies obtained from subtracting the 1st exciton peak energy from the 2nd exciton peak energy, but we do not divide by two (**Fig. 9**, black-diamonds). We extended the size-range using literature absorption spectra[43] (**Fig. 9**, red-diamonds). Next, we compare to

the Kang and Wise *k.p* calculated intraband transition energies ($1S_e$-$1P_e$) (**Fig. 9**, black-dashed-trace). There is good agreement at larger sizes, but deviate significantly at smaller QD diameters. The good agreement between these two estimates of the intraband transitions energy leads to the conclusion that the second exciton peak must be the dipole forbidden $1S_h$-$1P_e$/$1P_h$-$1S_e$ transition.

Here we attempt to resolve these contradictory observations. A recent calculation of the electronic structure of PbSe NRs by Bartnik et. al.[49] updated the Kang and Wise *k·p* calculations for spherical PbSe QDs. In their work they noted that to correctly calculate the transition energies for the first 8 exciton transitions, for a large range of PbSe QDs sizes, the anisotropy of the PbSe electronic bandstructure must be considered, which was not done for the Kang and Wise treatment. The anisotropy at the bandedge splits the P degenerate states into a set of transverse, $P^{\perp}$, and longitudinal, $P^{\parallel}$, states, as noted by Franceschetti et. al.[50] We extracted the calculated intraband energies of $P^{\parallel}$ and $P^{\perp}$as a function of QD size from Ref. 49 and present two traces in **Fig. 9**. First we plot the difference in the calculated S and $P^{\parallel}$ exciton energies (i.e., $(1P_h^{\parallel} \rightarrow 1P_e^{\parallel}) - (1S_h \rightarrow 1S_e)$, **Fig. 9**, black-trace), which represents the difference in energies between the 1st and 2nd exciton transitions. We then plot the difference in the calculated S and $P^{\perp}$ exciton energies and divide by 1.74 ($[(1P_h^{\perp} \rightarrow 1P_e^{\perp}) - (1S_h \rightarrow 1S_e)]/1.74$, the factor of 1.74 is to account for the differences in effective mass, **Fig. 9**, red-trace) to approximate the intraband $S_e \rightarrow P_e^{\perp}$ transition energy. We conclude that the difference between S and $P^{\parallel}$ exciton (black-trace and black triangles) only coincidentally is in-line with the calculated $S_e \rightarrow P_e^{\perp}$ transition energy (red-curve). In other words, the difference between 1st and 2nd exciton energies only coincidentally agree with intraband transition energies (and the agreement deviates for smaller QD sizes) because the $S_e \rightarrow P_e^{\perp}$ transition energy is about twice the $S_e \rightarrow P_e^{\parallel}$ transition energy. Therefore, the 2nd exciton transition should be assigned to the dipole allowed $1P_h^{\parallel} \rightarrow 1P_e^{\parallel}$ transition. While the observed intraband transition mainly arises from $S_e \rightarrow P_e^{\perp}$, instead of $S_e \rightarrow P_e^{\parallel}$ transition due its higher oscillator strength.[51]

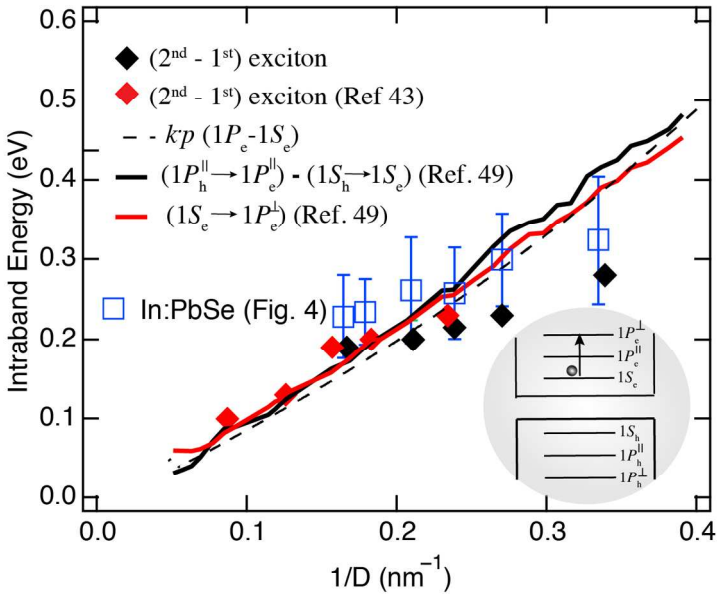

Figure 9. Size-dependent intraband energy $1S_e$–$1P_e$: The dashed-black trace is the $1S_e$-$1P_e$ transition energy calculated from the standard k·p theory of Kang and Wise. The black-trace is $1P^{\|}$exciton energy minus 1S exciton energy extracted from Ref. 49; the red-trace is an estimate of the $1S_e - 1P_e^{\perp}$ intraband transition energy, calculated from the different in energy of the 1S and $1P^{\perp}$excitons and divided by 1.74 to account for the differences in effective mass. Finally, we compare to subtracting the 1st exciton energy from the 2nd exciton energy obtained from the linear absorption spectra of the sample studied here (black-diamonds) and from literature[43] absorption spectra (red diamonds).

Next we discuss the deviation of the experimental energies of the intraband transitions in small size QDs to that predicted within the effective mass *k·p* models. In principle this disagreement can be connected with the difference between the average size of the QD contributing to the intraband absorption and average size of the QD ensemble. Indeed, one can show that the distribution density of intraband matrix element increases with size. This fact together with higher efficiency of the doping in larger QDs increases the average size of the QD contributing to the intraband absorption. This effect, however, cannot explain the difference between experiment and theory on our samples which have a very small size-dispersion (less than 5%). The phenomenon can be also connected with strongly localized resonant levels measured in bulk CdSe and CdTe semiconductors at energies ~ 300–400 meV above the edge of conduction band.[28-30] The levels originate from non-stochiometric defects, mainly vacancies, and early calculations of such levels where conducted by Volkov and Pankratov.[31,32] In small size QDs these resonant levels should interact with the $1P_e$ confined levels and their repulsion should slow down shift of the $1P_e$ state with a decrease of the QD size. However, existence of such levels in QDs has not been reported and additional theoretical and experimental investigation is required.

Conclusions

In this work, we present a facile method to prepare In^{3+}-doped PbSe QDs via a post-synthetic cation exchange technique. Quantitative XRD analysis suggests a substitutional doping mechanism, with the lattice parameters decreasing upon indium incorporation. A significant bleach of the first excitonic transition is observed in In:PbSe QDs, which is coupled with the appearance of a size-dependent intraband absorption in NIR, indicating a successful introduction of electron impurities in QDs. We also observe a decrease of PLQY and a faster exciton decay with higher In incorporation. An additional nonradiative relaxation pathway in In:PbSe QDs is introduced due to the In defects. Spectroelectrochemical measurements show a characteristic *n*-type behavior, which agrees with the substitutional doping mechanism of In^{3+} in PbSe. Additionally, it is found that the doping mechanism is highly reversible due to the high diffusivity of In in PbSe QDs. The demonstration of synthesizing *n*-type semiconductor nanocrystals in a controllable manner can further accelerate the development of such materials in numerous future applications such as solar cells, LEDs, and thermoelectrics.

Materials & Methods

A. Materials

All chemicals were used as received without further purification. Selenium (Se, 99.99%), oleic acid (90%), trioctylphosphine (TOP, 90%), diphenylphosphine (DPP, 98%), 1-octadecene (ODE, 90%), indium nitrate hydrate (99.99% trace metals basis), indium chloride (anhydrous, ≥99.999% trace metals basis), bis(cyclopentadienyl)cobalt(II) (cobaltocene), anhydrous methanol (MeOH, 99.8%), anhydrous ethanol (EtOH, 200 proof, ≥99.5%), nitric acid (TraceSELECT®, ≥69.0%), ultrapure water (TraceSelect® Ultra), anhydrous hexane (≥99%), anhydrous octane (≥99%), anhydrous tetrachloroethylene (TCE, ≥99.9%), anhydrous chloroform-d ($CDCl_3$, ≥99.8%), and ferrocene (Cp_2Fe, 98%), were purchased from Sigma-Aldrich and used as received. Lead oxide (PbO, 99.999%) was purchased from Alfa Aesar.

B. QD Synthesis and Purification

PbSe QDs were synthesized and purified using standard air-free techniques.[16] In a typical synthesis, a solution of 1.0 g PbO, 4 g oleic acid, and 11.6 g ODE was degassed in a 100 mL three-neck flask under vacuum and kept at 120°C for 1 hour. 15 mL of a 1 M TOP-Se solution containing 0.15 g DPP was then quickly injected into the Pb-oleate solution at various temperatures for a designated amount of time. The reaction was then quenched with a water bath and injection of 20 mL of hexanes, followed by three rounds of

precipitation/centrifugation/redissolution (PCR) purification using anhydrous hexane and ethanol. The purified QDs were stored as a powder in a nitrogen filled glovebox in the dark.

C. Solution Doping of PbSe QDs

The concentration of QDs each sample was first determined from the absorbance at 400 nm based on absorption spectroscopy (in TCE). The total number of lead atoms per sample can then be calculated assuming perfectly spherical and stoichiometric particles (detailed calculation can be found in the previous paper[16]). To the rapidly-stirred PbSe/hexanes solution, the necessary amount of indium nitrate solution (60 mM in anhydrous methanol, doping concentration varies from 1–8% In:Pb) was pipetted at room temperature. The reaction was allowed to proceed for 30 min before it was quenched by precipitating the QDs with excess ethanol. The sample was centrifuged at 8000 RPM for 10 mins and the supernatant was discarded. The In:PbSe QD solid was then resuspended in hexane for another round of PCR purification. Finally, the purified In:PbSe QD was stored as a powder in a nitrogen filled glovebox in the dark. In:PbSe QD powders were resuspended in octane for film formation or in TCE for optical characterization.

D. QD Film Preparation

a. XRD Analysis

Films were prepared for XRD by dropcasting undoped or solution doped In:PbSe QDs from hexane onto zero-diffraction Si substrates.

b. XPS/UPS Analysis

Thin films were prepared for XPS/UPS analysis *via* a spin-coating technique. Undoped or solution doped In:PbSe QD solutions (~20 mg/mL in octane) were deposited onto Au/Cr coated glass substrates and spun at 800 RPM for 30 s. The QDs are deposited for only one layer without any further ligand exchange.

c. DRIFTS Analysis

As synthesized PbSe QDs were dropcast onto Au/Cr coated Si substrates from concentrated hexane solution, followed by submerging the QD film in $InCl_3$/methanol solutions for varying amounts of time (ranging from 5 s to 10 min) to incorporate In^{3+} ions. Control experiments were carried by submerging the undoped QD films in cobaltacene/acetonitrile solutions.

E. Quantitative ^{1}H NMR

Quantitative ^{1}H NMR spectra were recorded on a Bruker Avance III 400 MHz instrument and acquired with sufficiently long delay (30 s) to allow complete relaxation between pulses. Undoped and solution doped In:PbSe QDs were dispersed in $CDCl_3$ with a known amount of ferrocene as an internal standard. With the combination of both UV-vis-NIR and ^{1}H NMR spectra, surface bound oleate ligand density can then be estimated using the well-resolved vinyl peak.

F. Inductively Coupled Plasma-Optical Emission Spectrometry (ICP-OES)

ICP-OES analysis was performed on an SPECTROBLUE ICP-OES. Undoped and In:PbSe QD samples were digested using concentrated nitric acid and diluted with ultrapure water for analysis.

G. UV-Vis-NIR Absorption Spectroscopy

Ground state optical absorbance spectra of undoped and In:PbSe QD samples suspended in TCE were collected using a Cary 500 UV-Vis-NIR spectrometer.

H. Photoluminescence Quantum Yield (PLQY) Spectroscopy

PLQY measurements for undoped and In:PbSe QD samples suspended in TCE were made using a previously established method.[52] QDs were dispersed in TCE with an absorbance of less than 0.1 OD at the excitation peak wavelength to minimize reabsorption effects. The measurements were taken in a LabSphere integration sphere with an 850 nm NIR-LED (ThorLabs M850L3) excitation source passed through an 850 nm centered 40 nm band-pass filter. Light from the sphere was fiber coupled to a customized fluorescence spectrometer consisting of a 900 nm long-pass filter, monochromator (PTI), and a two-stage thermocouple-cooled extended InGaAs detector. The excitation LED was driven by a 15 V square wave at 25 Hz using a Stanford Research Systems (SRS) DS335 function generator. The detector signal was amplified using a SRS SR530 lock-in amplifier, and all spectra were corrector for grating, fiber, integration sphere, and detector deficiencies using a calibrated lamp. The PL QY was calculated using:

$$PL\ QY = \frac{\int I_{sample}(\lambda) - I_{ref}(\lambda)\, d\lambda}{\int E_{ref}(\lambda) - E_{sample}(\lambda)\, d\lambda}$$

where 'I' indicates the measured intensity of the emitted light, 'E' indicates the measured intensity of the excitation light, 'sample' indicates measurements of QD samples, and 'ref' indicates measurements of a reference cuvette (contains pure solvent, TCE, without QDs).

I. Diffuse Reflectance Infrared Fourier Transform Spectroscopy (DRIFTS)

All of the DRIFTS absorbance measurements were conducted in Ar-filled glove box and were taken on a Bruker ALPHA FTIR Spectrometer using the DRIFTS sampling accessory with a resolution of 2 cm^{-1}. Clean Au/Cr coated Si substrates were used for background measurements.

J. Spectroelectrochemistry Measurements

Spectroelectrochemical experiments were carried out in a 1 cm^2 quartz cuvette with 0.1 M of lithium perchlorate salt in dry acetonitrile as the supporting electrolyte. A three-electrode configuration was used with a silver wire pseudoreference electrode, a Pt wire counter electrode, and the sample as the working electrode. Potentiostatic bias in increments of 50 mV was applied with a Princeton Applied Research Model 263 poteniostat interfaced with CorrWare software. Ferrocene was used an internal standard. UV-vis-NIR absorbance data were simultaneously recorded with an OceanFX spectrometer (Ocean Optics, UV-vis), and NIRQuest512-2.2 spectrometer (Ocean Optics, NIR). An Ocean Optics DH-2000-BAL was used as the light source. All spectroelectrochemical experiments were carried out in an argon filled glove box fitted with electrical and fiber optic pass-through junctions.
The change in absorbance with applied bias was calculated by subtracting the UV-vis-NIR spectrum at the open-circuit potential from the spectrum at a given applied potential. The open circuit potential was determined by allowing the electrode to equilibrate under galvanostatic conditions. Following the determination of V_{OC}, the maximum bleach in the negative region was determined by applying negative potential until the absorbance no longer changed. The electrochemical potential was the swept from negative to positive in 50 mV increments while recording the absorbance spectrum.

K. Transmission Electron Microscopy (TEM)

Transmission electron microscopy was performed using an FEI Tecnai G2 ST30 TEM operating at 300 kV. Samples were prepared by dropcasting undoped and solution doped In:PbSe QDs from dilute hexane solutions onto carbon coated copper grids.

L. X-Ray Diffraction (XRD)

Powder X-ray diffraction (XRD) data was collected using a Rigaku Ultima IV diffractometer in parallel beam geometry (2-mm beam width) using Cu *K*α radiation (λ = 1.54 Å). Samples were prepared by drop casting onto zero-diffraction, single crystal Si substrates.

Rietveld Analysis. Rietveld refinements of powder XRD patterns were performed using the General Structure Analysis System software (GSAS) with the graphical user interphase EXPGUI.[23,24] Crystal structures were refined using the cubic $Fm\bar{3}m$ space-group (no. 225). Atomic X-ray scattering factors were corrected for anomalous scattering. The following parameters were refined: (1) scale factor; (2) background, which was modeled using a shifted Chebyschev polynomial function; (3) peak shape, which was modeled using a Thompson–Cox–Hastings pseudo-Voigt function;[53] (4) lattice constant *a*; and (5) an isotropic displacement parameter for each atom in the structure ($U_{iso}^{Pb,In}$ and U_{iso}^{Se}). In:Pb ratios were fixed at the values obtained from elemental analysis. R_{wp} residuals and difference curves were employed to assess the quality of the refined structural models.

M. Photoelectron Spectroscopy

Photoelectron spectroscopy measurements were performed on a Physical Electronics, Inc. 5600 ESCA instrument. The XPS radiation is produced by a monochromatic Al (Kα) source centered at 1486.6 eV. The valence band spectra were taken with a step size of 0.05 eV and a pass energy of 5.85 eV. The electron binding energy scale was calibrated using the Fermi edge of cleaned metallic substrates (Au, Mo, Cu, and/or Ag), giving the spectra an uncertainty of ±0.05 eV. UPS measurements (He (Iα) = 21.22 eV) were taken with a step size of 0.025 eV and a pass energy of 2.95 eV. The UPS calibrations were done on the same cleaned substrates giving an energy uncertainty of ±0.025 eV.

N. Transient Absorption (TA)

Microsecond TA spectra were collected using Helios spectrometer (Ultrafast systems). A Coherent Libra regeneratively amplified Ti:sapphire laser with ~4 W, 1 kHz, and ~100 fs pulse width output at 800 nm is used for pump beam generation. The 800 nm beam is directed into a TOPAS optical parametric amplifier to generate pump pulse and is modulated at 500 Hz through an optical chopper to block every other laser pulse. The probe beam is derived from EOS system and is electronically delayed respect to pump laser pulse. The probe beam produced is a broadband Vis-NIR spectrum from 800-1600 nm. The probe then is passed through a

continuously variable neutral density filter and a fraction is separated off to be used as a reference that accounts for probe beam intensity fluctuations. The pump and probe beams are then overlapped at the sample. NIR photodiode arrays (Ultrafast Systems) are used to detect the probe and reference beams for data acquisition.

Acknowledgements

We acknowledge support from the Center for Advanced Solar Photophysics (CASP), an Energy Frontier Research Center funded by the US Department of Energy, Office of Science, Office of Basic Energy Sciences. The Spectroelectrochemical and XPS measurements were supported by the Solar Photochemistry Program within the Division of Chemical Sciences, Geosciences and Biosciences, Office of Basic Energy Sciences, Office of Science within the US Department of Energy. Part of this work was authored by Alliance for Sustainable Energy, LLC, the manager and operator of the National Renewable Energy Laboratory for the U.S. Department of Energy (DOE) under Contract No. DE-AC36-08GO28308. D.K.A. and F.A.R. acknowledge the support provided by Wayne State University and by the Research Corporation for Science Advancement through a Cottrell Scholar Award for the Rietveld Analysis. ALE acknowledges financial support of the Office of Naval Research (ONR) through the Naval Research Laboratory Basic Research Program. The views expressed in the article do not necessarily represent the views of the DOE or the U.S. Government. The U.S. Government retains and the publisher, by accepting the article for publication, acknowledges that the U.S. Government retains a nonexclusive, paid-up, irrevocable, worldwide license to publish or reproduce the published form of this work, or allow others to do so, for U.S. Government purposes.

Supporting Information

1H NMR spectroscopy data, elemental analysis, Rietveld refinements, photoelectron spectroscopy data, control absorbance measurements

References

(1) Shklovskii, B. I.; Efros, A. L.: *Electronic Properties of Doped Semiconductors*; Springer Science & Business Media: Berlin, 2013.

(2) Schimpf, A. M.; Knowles, K. E.; Carroll, G. M.; Gamelin, D. R. *Acc. Chem. Res.* **2015**, *48*, 1929-1937.

(3) Shim, M.; Guyot-Sionnest, P. *Nature* **2000**, *407*, 981.

(4) Koh, W. K.; Koposov, A. Y.; Stewart, J. T.; Pal, B. N.; Robel, I.; Pietryga, J. M.; Klimov, V. I. *Sci. Rep.* **2013**, *3*, 2004.

(5) Palomaki, P. K. B.; Miller, E. M.; Neale, N. R. *J. Am. Chem. Soc.* **2013**, *135*, 14142-14150.

(6) Haase, M.; Weller, H.; Henglein, A. *J. Phys. Chem.* **1988**, *92*, 482-487.

(7) Rinehart, J. D.; Schimpf, A. M.; Weaver, A. L.; Cohn, A. W.; Gamelin, D. R. *J. Am. Chem. Soc.* **2013**, *135*, 18782-18785.

(8) Schimpf, A. M.; Lounis, S. D.; Runnerstrom, E. L.; Milliron, D. J.; Gamelin, D. R. *J. Am. Chem. Soc.* **2015**, *137*, 518-524.

(9) Faucheaux, J. A.; Jain, P. K. *J. Phys. Chem. Lett.* **2013**, *4*, 3024-3030.
(10) Wang, C.; Shim, M.; Guyot-Sionnest, P. *Science* **2001**, *291*, 2390.
(11) Wehrenberg, B. L.; Guyot-Sionnest, P. *J. Am. Chem. Soc.* **2003**, *125*, 7806-7807.
(12) Liu, H.; Keuleyan, S.; Guyot-Sionnest, P. *J. Phys. Chem. C* **2012**, *116*, 1344-1349.
(13) Sahu, A.; Kang, M. S.; Kompch, A.; Notthoff, C.; Wills, A. W.; Deng, D.; Winterer, M.; Frisbie, C. D.; Norris, D. J. *Nano Lett.* **2012**, *12*, 2587-2594.
(14) Stavrinadis, A.; Rath, A. K.; de Arquer, F. P.; Diedenhofen, S. L.; Magen, C.; Martinez, L.; So, D.; Konstantatos, G. *Nat. Commun.* **2013**, *4*, 2981.
(15) Wills, A. W.; Kang, M. S.; Wentz, K. M.; Hayes, S. E.; Sahu, A.; Gladfelter, W. L.; Norris, D. J. *J. Mater. Chem.* **2012**, *22*, 6335-6342.
(16) Kroupa, D. M.; Hughes, B. K.; Miller, E. M.; Moore, D. T.; Anderson, N. C.; Chernomordik, B. D.; Nozik, A. J.; Beard, M. C. *J. Am. Chem. Soc.* **2017**, *139*, 10382-10394.
(17) Buonsanti, R.; Milliron, D. J. *Chem. Mater.* **2013**, *25*, 1305-1317.
(18) Galli, G. *Nature* **2005**, *436*, 32.
(19) Erwin, S. C.; Zu, L.; Haftel, M. I.; Efros, A. L.; Kennedy, T. A.; Norris, D. J. D *Nature* **2005**, *436*, 91.
(20) Tabatabaei, K.; Lu, H.; Nolan, B. M.; Cen, X.; McCold, C. E.; Zhang, X.; Brutchey, R. L.; van Benthem, K.; Hihath, J.; Kauzlarich, S. M. *Chem. Mater.* **2017**, *29*, 7353-7363.
(21) Hassinen, A.; Moreels, I.; De Nolf, K.; Smet, P. F.; Martins, J. C.; Hens, Z. *J. Am. Chem. Soc.* **2012**, *134*, 20705-20712.
(22) Anderson, N. C.; Hendricks, M. P.; Choi, J. J.; Owen, J. S. *J. Am. Chem. Soc.* **2013**, *135*, 18536-18548.
(23) Larson, A. C.; Von Dreele, R. B.: *General Structure Analysis System (GSAS)*; Los Alamos National Laboratory, 2000.
(24) Toby, B. EXPGUI, a graphical user interface for GSAS. *J. Appl. Cryst.* **2001**, *34*, 210-213.
(25) Araujo, J. J.; Brozek, C. K.; Kroupa, D. M.; Gamelin, D. R. *Nano Lett.* **2018**, *18*, 3893-3900.
(26) Kang, I.; Wise, F. W. *J. Opt. Soc. Am. B* **1997**, *14*, 1632.
(27) Diaconescu, B.; Padilha, L. A.; Nagpal, P.; Swartzentruber, B. S.; Klimov, V. I. *Phys. Rev. Lett.* **2013**, *110*, 127406.
(28) Kucherenko, I. V.; Pankratov, O. A.; Svistov, A. E.; Chizhevskii, E. G.; Shotov, A. P. *Sov. Phys. Semicond.* **1984**, *18*, 991-994.
(29) Baleva, M. I.; Maksimov, M. H.; Sendova, M. S. *J. Phys. C: Solid State Phys.* **1987**, *20*, 941.
(30) S. Itskevich, E.; M. Kashirskaya, L.; Kucherenko, I.; Pankratov, O.; E. Svistov, A.; P. Shotov, A.: *Pressure-induced inversion of the Hall coefficient and the thermal emf in narrow-gap lead-tin-selenium semiconductors*, **1986**; *43*.
(31) Pankratov, O. A.; Povarov, P. P. *Solid State Commun.* **1988**, *66*, 847-853.
(32) Volkov, B. A.; Pankratov, O. A. *Sov. Phys. JETP* **1985**, *61*, 164-171.
(33) Wehrenberg, B. L.; Yu, D.; Ma, J.; Guyot-Sionnest, P. *J. Phys. Chem. B* **2005**, *109*, 20192-20199.
(34) Schimpf, A. M.; Knowles, K. E.; Carroll, G. M.; Gamelin, D. R. *Acc. Chem. Res.* **2015**, *48*, 1929-1937.

(35) Kroupa, D. M.; Vörös, M.; Brawand, N. P.; McNichols, B. W.; Miller, E. M.; Gu, J.; Nozik, A. J.; Sellinger, A.; Galli, G.; Beard, M. C. *Nat. Commun.* **2017**, *8*, 15257.

(36) Liu, H.; Brozek, C. K.; Sun, S.; Lingerfelt, D. B.; Gamelin, D. R.; Li, X. *J. Phys. Chem. C* **2017**, *121*, 26086-26095.

(37) Carroll, G. M.; Tsui, E. Y.; Brozek, C. K.; Gamelin, D. R. *Chem. Mater.* **2016**, *28*, 7912-7918.

(38) Jeong, K. S.; Deng, Z.; Keuleyan, S.; Liu, H.; Guyot-Sionnest, P. *J. Phys. Chem. Lett.* **2014**, *5*, 1139-1143.

(39) Chen, X.; Choing, S. N.; Aschaffenburg, D. J.; Pemmaraju, C. D.; Prendergast, D.; Cuk, T. *J. Am. Chem. Soc.* **2017**, *139*, 1830-1841.

(40) Chen, D.; Viswanatha, R.; Ong, G. L.; Xie, R.; Balasubramaninan, M.; Peng, X. T. *J. Am. Chem. Soc.* **2009**, *131*, 9333-9339.

(41) Yang, L.; Knowles, K. E.; Gopalan, A.; Hughes, K. E.; James, M. C.; Gamelin, D. R. *Chem. Mater.* **2016**, *28*, 7375-7384.

(42) Hughes, K. E.; Hartstein, K. H.; Gamelin, D. R. *ACS Nano* **2018**, *12*, 718-728.

(43) Koole, R.; Allan, G.; Delerue, C.; Meijerink, A.; Vanmaekelbergh, D.; Houtepen Arjan, J. *Small* **2008**, *4*, 127-133.

(44) Wehrenberg, B. L.; Wang, C.; Guyot-Sionnest, P. *J. Phys. Chem. B* **2002**, *106*, 10634.

(45) Koh, W. K.; Koposov, A. Y.; Stewart, J. T.; Pal, B. N.; Robel, I.; Pietryga, J. M.; Klimov, V. I. *Sci. Rep.* **2013**, *3*.

(46) Peterson, J. J.; Huang, L.; Delerue, C.; Allan, G.; Krauss, T. D. *Nano Lett.* **2007**, *7*, 3827-3831.

(47) Liljeroth, P.; van Emmichoven, P. A. Z.; Hickey, S. G.; Weller, H.; Grandidier, B.; Allan, G.; Vanmaekelbergh, D. *Phys. Rev. Lett.* **2005**, *95*, 086801.

(48) Trinh, M. T.; Houtepen, A. J.; Schins, J. M.; Piris, J.; Siebbeles, L. D. A. *Nano Lett.* **2008**, *8*, 2112-2117.

(49) Bartnik, A. C.; Efros, A. L.; Koh, W. K.; Murray, C. B.; Wise, F. W. E. *Phys. Rev. B* **2010**, *82*.

(50) Franceschetti, A.; Luo, J. W.; An, J. M.; Zunger, A. *Phys. Rev. B* **2009**, *79*, 241311.

(51) An, J. M.; Franceschetti, A.; Dudiy, S. V.; Zunger, A. T. *Nano Lett.* **2006**, *6*, 2728-2735.

(52) Semonin, O. E.; Johnson, J. C.; Luther, J. M.; Midgett, A. G.; Nozik, A. J.; Beard, M. C. *J. Phys. Chem. Lett.* **2010**, *1*, 2445-2450.

(53) Thompson, P.; Cox, D. E.; Hastings, J. B. *J. Appl. Cryst.* **1987**, *20*, 79-83.